Supporting Information

Brookes et al. 10.1073/pnas.1112685108

SI Materials and Methods

Beamformer Application, Hilbert Envelope Computation, and Independent Component Analysis: Examples in a Two-Back Working Memory Experiment. In this section, the algebraic formulations of beamformer application, Hilbert envelope computation, and ICA are given. Examples of Hilbert envelope time courses from network nodes of interest, along with temporal independent component time courses, are also given. All results shown are derived from resting state data presented in *SI Materials and Methods*.

Beamforming. Using a beamformer spatial filter, an estimate of electrical source strength $\widehat{Q}_{\boldsymbol{\theta}}(t)$, made at time t and a predetermined location in the brain, is given by a weighted sum of sensor measurements; thus

$$\widehat{Q}_{\boldsymbol{\theta}}(t) = \mathbf{W}_{\boldsymbol{\theta}}^T \mathbf{m}(t), \qquad \textbf{[S1]}$$

(1–3), where $\mathbf{m}(t)$ is a vector of magnetic field measurements made at time t, and $\mathbf{W}_{\boldsymbol{\theta}}$ is a vector of weighting parameters tuned to a predefined source space location and current orientation. Location and orientation are represented here by a six-element vector $\boldsymbol{\theta}$. The superscript T indicates a matrix transpose.

The weighting parameters $(\mathbf{W}_{\boldsymbol{\theta}})$ are derived on the basis of power minimization. The overall power in the output signal $\widehat{Q}_{\boldsymbol{\theta}}(t)$ is minimized with the linear constraint that power originating from the location/orientation of interest $(\boldsymbol{\theta})$ remains. Mathematically the beamformer problem is formulated as

$$\min_{\mathbf{W}_{\boldsymbol{\theta}}}\left[\widehat{Q}_{\boldsymbol{\theta}}^2\right] \text{ subject to } \mathbf{W}_{\boldsymbol{\theta}}^T \mathbf{L}_{\boldsymbol{\theta}} = 1, \qquad \textbf{[S2]}$$

where $\widehat{Q}_{\boldsymbol{\theta}}^2$ represents source power and is given by $\widehat{Q}_{\boldsymbol{\theta}}^2 = \mathbf{W}_{\boldsymbol{\theta}}^T \mathbf{C} \mathbf{W}_{\boldsymbol{\theta}}$. $\mathbf{C}$ represents the data covariance matrix calculated over a time-frequency window of interest, and $\mathbf{L}_{\boldsymbol{\theta}}$ is the lead field vector, which is a vector containing the magnetic fields that would be measured at each of the MEG sensors in response to a source of unit amplitude with location and orientation specified by $\boldsymbol{\theta}$. Throughout *SI Materials and Methods*, $\mathbf{L}_{\boldsymbol{\theta}}$ is based on a dipolar model of neuronal current (4). The solution to Eq. **S2** is found analytically and given by

$$\mathbf{W}_{\theta}^T = \left[\mathbf{L}_{\theta}^T \{\mathbf{C} + \mu\Sigma\}^{-1} \mathbf{L}_{\theta}\right]^{-1} \mathbf{L}_{\theta}^T \{\mathbf{C} + \mu\Sigma\}^{-1}. \qquad \textbf{[S3]}$$

$\boldsymbol{\Sigma}$ is a diagonal matrix representing the white noise at each of the MEG channels and μ is a Backus–Gilbert regularization parameter and is used to adjust the trade-off between the full width at half maximum of the point spread function of the final beamformer image (i.e., spatial resolution) and the magnitude of uncorrelated noise in the time-course reconstruction. In this work we set $\mu = 4$ to ensure high SNR in reconstructed time courses and thus give us the best opportunity to observe temporal correlation. This method also increased spatial smoothness before concatenation across subjects to lessen the effect of spatial misregistration. More specifically, the value of 4 was taken from previously published work (5).

Here, time series $\widehat{Q}_{\boldsymbol{\theta}}(t)$ were reconstructed for a set of locations placed at the vertices of a regular 5-mm grid spanning the entire brain. The orientation of each source was based on a nonlinear search for the orientation of maximum signal to noise ratio, Z_{opt} such that mathematically we compute

$$Z_{\text{opt}} = \max_{\delta}\left(\frac{\mathbf{W}_{\boldsymbol{\theta}}^T \mathbf{C} \mathbf{W}_{\boldsymbol{\theta}}}{\mathbf{W}_{\boldsymbol{\theta}}^T \Sigma \mathbf{W}_{\boldsymbol{\theta}}}\right), 0^{\circ} \leq \delta \leq 180^{\circ}, \qquad \textbf{[S4]}$$

where δ is the angle of the source orientation in the tangential plane with respect to the azimuthal direction and we assume that $\boldsymbol{\theta} = (\mathbf{r}, \delta)$. This process is equivalent to the scalar beamformer implementation, also known as synthetic aperture magnetometry (SAM).

Hilbert envelope computation. Having computed beamformer reconstructed time series, $\widehat{Q}_{\boldsymbol{\theta}}(t)$, for each source space voxel, the corresponding *analytic signal* $z_{\theta}(t)$ is given by

$$z_{\theta}(t) = Q_{\theta}(t) + iH(Q_{\theta}(t)), \qquad \textbf{[S5]}$$

where $H(Q_{\theta}(t))$ represents the Hilbert transform of $Q_{\theta}(t)$ and is given by

$$H[Q_{\theta}(t)] = P\left[\frac{1}{\pi}\int_{-\infty}^{\infty} \frac{Q_{\theta}(u)}{t-u} du\right], \qquad \textbf{[S6]}$$

where P denotes the Cauchy principal value of the integral and is used to take account of the singularity at $t = u$. This integral effectively represents a convolution of $Q_{\theta}(t)$ with $1/\pi t$. The magnitude of the analytic signal is defined in Eq. **S7**, and this signal yields the envelope of the measured oscillatory activity in $Q_{\theta}(t)$:

$$E(Q_{\theta}(t)) = \sqrt{(Q_{\theta}(t))^2 + (H(Q_{\theta}(t)))^2}. \qquad \textbf{[S7]}$$

Throughout *SI Materials and Methods*, $E(Q_{\theta}(t))$ is referred to as the Hilbert envelope signal. Hilbert envelopes were temporally down-sampled to an effective sampling resolution of 1 s before ICA.

Fig. S1 shows example temporally down-sampled Hilbert envelope signals, extracted from locations of interest in three separate networks, motor, visual, and left and right frontoparietal (FP). Locations were defined on the basis of fMRI data presented in the main text. Results are shown for a single subject. Because these Hilbert envelope time courses represent resting state data, no temporal features of interest are distinguishable. However, note reasonable temporal correlation between time courses from spatially separate nodes of the same network. These temporal data form the basis of the results shown in Fig. 2 of the main text.

Independent component analysis. Before ICA, Hilbert envelope signals from all spatial locations within the brain were temporally down-sampled to an effective time resolution of 1 s. The resulting spatiotemporal data were transformed to standard (MNI) space using FLIRT in FSL, and the voxel size was resampled to an 8-mm grid. A matrix was formed in which each row represented the down-sampled Hilbert envelope time course, from a separate voxel in the brain, concatenated across subjects. Mathematically,

$$X = \begin{bmatrix} E\left(Q_{r_1}^{(\text{subject }1)}(t)\right), E\left(Q_{r_1}^{(\text{subject }2)}(t)\right), \ldots \\ E\left(Q_{r_2}^{(\text{subject }1)}(t)\right), E\left(Q_{r_2}^{(\text{subject }2)}(t)\right), \ldots \\ \cdots \\ E\left(Q_{r_N}^{(\text{subject }1)}(t)\right), E\left(Q_{r_N}^{(\text{subject }2)}(t)\right), \ldots \end{bmatrix}, \qquad \textbf{[S8]}$$

where r_1, r_2, etc. represent the different brain space locations, N is the total number of voxels, and the superscripts (in parentheses) indicate subject number. Before concatenation time courses were mean corrected and variance normalized. Temporal ICA was then applied such that the measurements, **X**, were defined as linear mixtures of temporally independent signals **S**,

$$\mathbf{X} = \mathbf{AS}, \qquad \textbf{[S9]}$$

where **A** is the mixing matrix that defines the contribution of each independent temporal signal to each voxel time course. The unmixing matrix, **W**, was estimated giving the contribution of each voxel time course to each independent component:

$$\widehat{\mathbf{S}} = \mathbf{WX}. \qquad \textbf{[S10]}$$

Temporal independent components were estimated using the fastICA algorithm in matlab [research.ics.tkk.fi/ica/fastica]. Before ICA, prewhitening was applied to reduce the dataset to 30 principal components. Twenty-five independent components were derived. The spatial signature of each tIC (i.e., the maps shown in Fig. 1) was measured by Pearson correlation between the tIC and the time course of each voxel in the concatenated dataset. This process was implemented independently for each frequency band of interest.

Fig. S2 shows examples of temporal independent components from four brain networks extracted using ICA: motor (Fig. S2*A*), visual (Fig. S2*B*), left FP (Fig. S2*C*), and right FP (Fig. S2*D*). The temporal independent component (IC) signal is shown in green. The raw Hilbert envelope signals, extracted from separate nodes of those networks (i.e., those signals presented in Fig. S1) are shown in black. Time courses have been mean corrected and normalized by their maximal value for display. Again, because these signals represent resting state data, no temporal features are apparent. However, note reasonable temporal agreement between raw signals and the tICs.

Other Independent Components Extracted from Resting State Data. The main text shows ICs that were found to spatially match those observed in fMRI; however, this number comprised only 7 of 25 components computed in the β-band. Here, 11 further components are shown. As in the main text the overlay represents correlation between the IC time course and time courses for each voxel, thresholded at a Pearson correlation coefficient of 0.3. Components not shown did not correlate with any voxel above the threshold.

Fig. S3 shows the spatial structure of the remaining β-band–independent components. Some of these patterns implicate only a single brain region, whereas others highlight plausible brain networks. It is interesting to note cross-hemisphere symmetry across multiple components; for example, left and right insula cortices are observed spread across two components (Fig. S3 *B* and *C*, respectively). Likewise left and right sensorimotor areas are spread across components in Fig. S3 *E* and *F*. However, the direct functional relevance of these components remains unclear and if such patterns are consistent across MEG datasets, they may warrant further investigation.

Statistical Significance of Spatial Correlation. Fig. 1 of the main text shows spatial similarity in RSNs identified independently using MEG and fMRI. Spatial matching of these maps across modalities was achieved quantitatively using a *spatial Pearson correlation coefficient* measure. Here, 3D maps were reshaped into 1D vectors, elements representing spatial locations outside the brain were removed, and the correlation coefficient between MEG- and fMRI-derived vectors was computed to give a numerical estimate of spatial similarity. Maps with the largest correlation coefficients were paired.

The statistical significance of spatial correlations was assessed using a Monte Carlo approach. Initially 10 MEG measurements were made, each comprising 300 s of data (recorded using the third-order gradiometer configuration of the 275-channel system at a sampling rate of 600 Hz) with no subject in the scanner. These "empty room" data were filtered into the appropriate frequency bands and projected into brain space using *the same* spatial filters as those used to project real MEG data. (Each of the 10 empty room measurements was projected using spatial filters derived from a different individual). This process ensured that any spatial structure introduced to the real data by the spatial filters was also introduced to the empty room data. Following projection, Hilbert envelopes were computed and down-sampled to a 1-s time resolution, and data were smoothed spatially, transformed to MNI space, and concatenated, yielding a noise dataset equivalent to the real data used to generate Fig. 1. Following this, a Monte Carlo approach was adopted. On each iteration of the algorithm, independent component analysis was applied to the noise dataset, yielding 25 spatial maps, equivalent to those in Fig. 1 but whose spatial signature was independent of recorded brain activity. The spatial Pearson correlation coefficient between each of these 25 "fake" maps and the eight RSNs identified using fMRI and shown in Fig. 1 was computed. The maximum correlation across all 25 independent components was also logged. Four hundred iterations of this algorithm were run, across which data segments were randomly switched in time. This process yielded a total of 10,000 fake correlation coefficients and 400 "maximum" correlation coefficients representing the best spatial match to each of the fMRI-derived RSNs for each ICA computation. To enable a direct comparison of the fake spatial correlation coefficient distributions for each network, with equivalent spatial correlation coefficients derived from the real data, the spatial Pearson correlation coefficients were also computed between the fMRI- and MEG-derived RSNs. This procedure was done for 20 repeats of ICA applied to real data.

Fig. S4 shows the results. The blue curve shows the statistical distribution of fake spatial correlation coefficients. The green curve shows the distribution of the highest correlation coefficient for each ICA iteration. The red line shows the mean spatial correlation coefficient derived from real data; the gray shaded area shows SD across 20 ICA iterations for real data. Results for DMN, left lateral FP network, right lateral FP network, motor network, medial parietal regions, visual network, frontal lobes, and cerebellum are shown. Note that because the spatial signatures of the networks are different, the statistical test was applied to each network individually. This approach was expected to be more conservative. Statistical values were derived empirically from the distributions of the maximal correlation (i.e., the green curves) as this method eliminates the need to correct for multiple comparisons. Spatial correlation was significant ($P < 0.05$) for all networks apart from the cerebellum for which there was generally high correlation between the ICs derived from empty room data and the fMRI-derived network. However, the real spatial correlation between modalities for this network is confounded because limited coverage in fMRI meant a "cutoff" in the lower half of the cerebellum. This result can be seen clearly in Fig. 1.

Connectivity Spectra in the Motor and Visual Networks. Fig. 3 of the main text show envelope correlation measurements applied between nodes of the default mode and left/right lateralized frontoparietal networks. For completeness here we show equivalent measurements in the motor network and the visual network.

Fig. S5 shows that significant connectivity is observed between the left and right primary sensorimotor areas and this observation is in agreement with previously published results. Connectivity is mediated by β-band oscillations. Hilbert envelope correlation between the left and right primary visual areas did not reach significance according to our simulation approach. This result is due to crosstalk between spatial filters for those two locations.

The left and right visual areas were separated by just 32 mm. Significant signal leakage between these two locations is evidenced by high levels of Hilbert envelope correlation in the simulated data (green line) and we should therefore conclude that any real connectivity that exists between these two locations is being masked by crosstalk between spatial filters. This conclusion exemplifies the principal limitation of MEG connectivity metrics and the importance of testing for spurious correlation.

Resting State Neural Oscillatory Power Spectra. Here, for a number of nodes of interest in the networks presented, we compute resting state spectra showing the distribution of oscillatory amplitude as a function of frequency. For each band, the amplitude spectrum value is computed as the mean value of the Hilbert envelope in that frequency band over the entire 5-min resting state recording. Values are averaged over subjects and mean ± SE is reported.

In general, there is similarity across spectra derived from different locations with the largest amplitudes in the α- and β-bands. However, note the subtle differences in the spectra: Neural oscillations in the frontal areas are characterized by a bimodal spectrum with clearly separate peaks in the θ- and the high–β-frequency bands. Oscillations in the motor areas are strongest in the β-band; this result is not surprising given the well-characterized role of β-oscillations in motor tasks. Parietal cortices exhibit strong oscillatory activity in both the α- and low β-bands whereas visual cortex exhibits an α-band peak as would be expected (6). Finally, note the demarcation between the primary visual cortex and the cerebellum, suggesting that activity in cerebellum is not a result of signal leakage from the occipital regions but genuinely represents a separate pattern of activity from this region.

Of most interest is the difference between amplitude spectra and correlation spectra shown in Fig. 3 and Fig. S6*A*. In the left and right FP networks (Fig. S6 *D* and *E*) and the default mode network (Fig. S6*A*) clear θ-band components are observed in the amplitude spectra, but not the correlation spectra (Fig. 3), indicating that despite the prevalence of θ-oscillations, they are not involved in frontoparietal or default mode connectivity. Likewise note the demarcation between the connectivity spectrum and the power spectra shown for the motor network (compare Figs. S5*A* and S6*B*). Despite the prevalence of 8- to 13-Hz oscillatory activity in both primary sensorimotor regions, no significant correlation is observed between the Hilbert envelopes in this frequency band.

Consistency of Resting State Networks. To test the consistency of the spatial structure of the networks identified in Fig. 1, a separate MEG dataset was used. The new dataset comprised 300-s resting state recordings made in 14 subjects. In 7 subjects, resting state data were recorded before a motor task; in the remaining 7, resting state data were recorded before our working memory (two-back) task. In both cases the 300-s rest and the task-positive data were contiguous. As before, MEG data were recorded using the third-order synthetic gradiometer configuration of a 275-channel CTF system at a sampling rate of 600 Hz with a 150-Hz low-pass anti-aliasing hardware filter. Localization of the subject's head within the MEG helmet and coregistration of sensor locations to the brain anatomy were achieved as described in the main text. Processing of MEG data was also equivalent to that described in *Materials and Methods*: Data were projected to source space using a beamformer; for each voxel the Hilbert envelope was computed and temporally down-sampled to a 1-s resolution; and data for all subjects were smoothed spatially (FWHM 5 mm), transformed to MNI space, and concatenated temporally. Temporal ICA was applied using fastICA: Prewhitening was applied before ICA to reduce the dataset to 30 principal components. Twenty-five independent components were derived. Because results in Fig. 1 used only α- and β-band–filtered MEG data, only these two frequency bands were analyzed.

Results of ICA on the 14-subject dataset are compared with those generated from the original 10-subject dataset in Fig. S7. Fig. S7 *A–H* shows the default mode network, the left lateral frontoparietal network, the right lateral frontoparietal network, the motor network, medial parietal regions, the visual network, frontal lobes, and cerebellum, respectively. Fig. S7 *A–H*, *Upper* shows the original result and Fig. S7 *A–H*, *Lower* shows the best spatial match in the comparison dataset. Note that the default mode network (Fig. S7*A*) was found in the α-band whereas all other networks shown were in the β-band. In general we note qualitative agreement between networks observed using both datasets. Whereas the quality of the spatial match differed across components, the brain areas implicated were unambiguously matched for all eight independent components shown in Fig. 1. Differences between datasets could be the result of artifacts in MEG data including environmental interference and biomagnetic sources of no interest. Alternatively, they could reflect genuine differences induced by experimental method; because in the comparison dataset resting data were recorded contiguously with task-positive data, subjects were anticipating the start of a task during the 300-s rest. This observation could conceivably bring about changes in network measurements.

Fig. S8 shows temporal correlation measurements made between the IC time course of the DMN (α-band) and that of all of the other networks (identified in the β-band). Fig. S8, *Upper* shows the result for the original data (equivalent to Fig. 3*C* in the main text); Fig. S8, *Lower* shows an equivalent result derived from the comparison dataset. Once again a degree of synergy is observed between these two results and both exhibit some agreement with the equivalent result derived from fMRI data shown in Fig. 3*C*. Specifically, for both MEG datasets (and for fMRI) the largest temporal agreement is observed between DMN and the left frontoparietal, right frontoparietal, and medial frontal networks. Once again, differences between measurements could be the result of artifacts in MEG data or reflect genuine differences brought about by experimental method. This is an area for future study.

This paper has reported the application of beamformer spatial filtering and independent component analysis to MEG data to extract the spatiotemporal signature of electrophysiological resting state brain networks. The results presented, in particular the agreement between MEG- and fMRI-based RSN measurements, make the paper compelling. Also, this method is a unique use of ICA in combination with beamformer spatial filtering. Our work paves the way for further studies to explore this method, in particular the large parameter space that is implicated. The impacts of changing parameters such as beamformer regularization, noise normalization, temporal down-sampling, spatial smoothing, and ICA methodology are, as yet, unknown. In addition, it is likely that the beamformer/ICA technique will find application in task-positive studies. This initial work therefore opens up hitherto unexplored avenues of research.

1. Gross J, et al. (2001) Dynamic imaging of coherent sources: Studying neural interactions in the human brain. *Proc Natl Acad Sci USA* 98:694–699.
2. Robinson S, Vrba J (1998) Functional neuroimaging by synthetic aperture magnetometry. *Recent Advances in Biomagnetism*, eds Yoshimoto T, Kotani M, Kuriki S, Karibe H, Nakasato N (Tohoku Univ Press, Sendai, Japan), pp 302–305.
3. Van Veen BD, van Drongelen W, Yuchtman M, Suzuki A (1997) Localization of brain electrical activity via linearly constrained minimum variance spatial filtering. *IEEE Trans Biomed Eng* 44:867–880.
4. Sarvas J (1987) Basic mathematical and electromagnetic concepts of the biomagnetic inverse problem. *Phys Med Biol* 32:11–22.

5. Brookes MJ, et al. (2011) Measuring functional connectivity using MEG: Methodology and comparison with fcMRI. *Neuroimage* 56:1082–1104.

6. Berger H (1929) Uber das elektrenephalogramm des menschen. *Arch Psychiatr Nervenkr* 87:527–570.

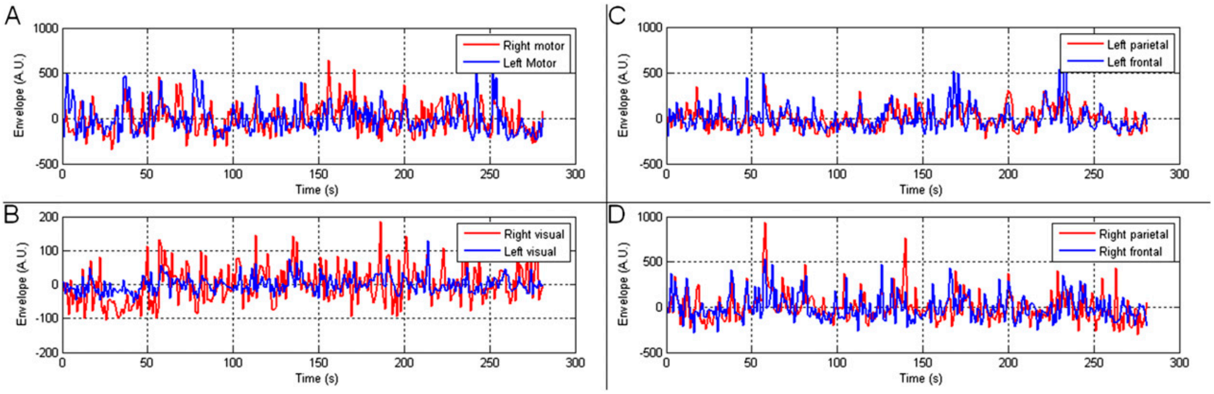

Fig. S1. Examples of Hilbert envelope time courses extracted from four networks: motor (*A*), visual (*B*), left FP (*C*), and right FP (*D*). Signals have been mean corrected.

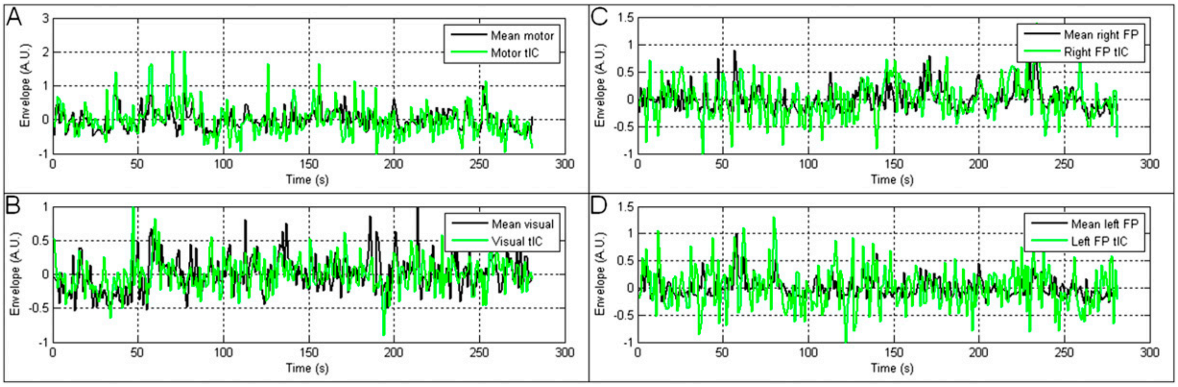

Fig. S2. Temporal signature of four resting state networks: motor (*A*), visual (*B*), Left FP (*C*), and right FP (*D*).

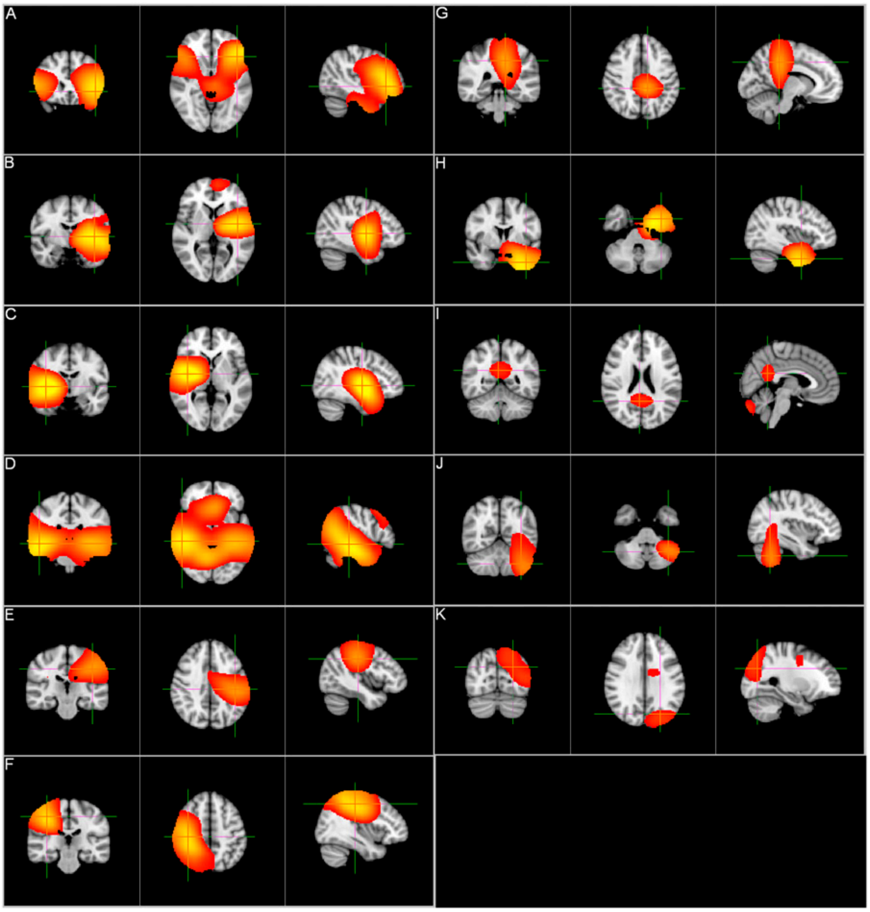

Fig. S3. *A–K* show 11 separate independent components found in the β-band that were not found to spatially match fMRI-based networks.

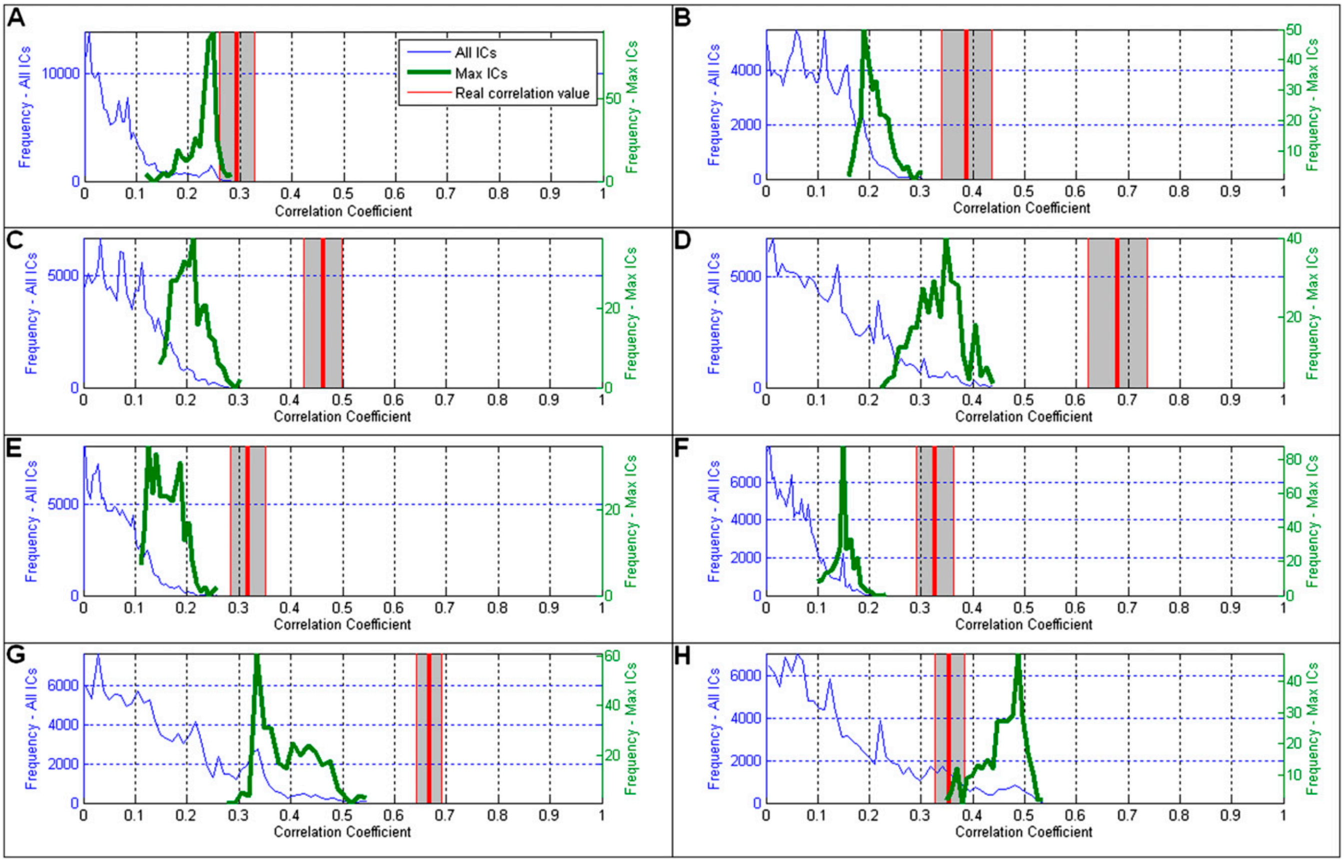

Fig. S4. Assessment of the statistical significance of spatial correlation. The blue line shows the statistical distribution of spatial correlation coefficients derived from 400 iterations of the ICA algorithm applied to MEG noise data. The green line shows the highest correlation for each iteration of ICA. The red line shows the mean spatial correlation coefficient derived from 20 iterations of ICA applied to the real data; the gray shaded area shows SD across these 20 iterations. *A*–*H* show results for the default mode network, the left lateral frontoparietal network, the right lateral frontoparietal network, the motor network, medial parietal regions, the visual network, frontal lobes, and cerebellum, respectively.

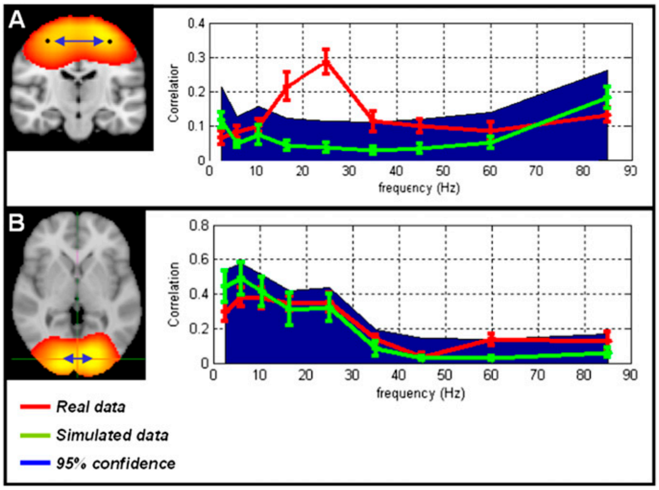

Fig. S5. Connectivity spectra in (*A*) the motor network and (*B*) the visual system.

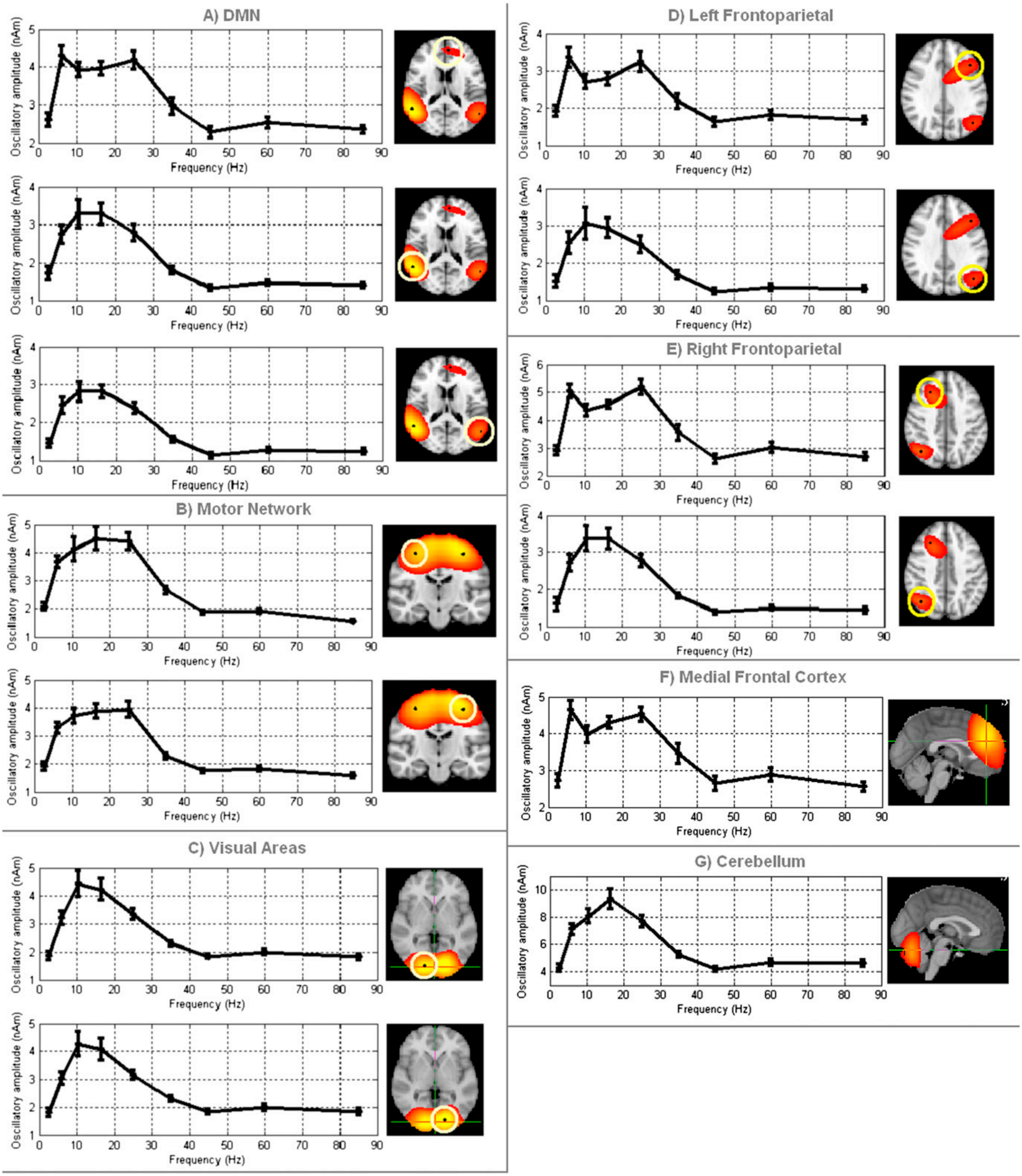

Fig. S6. Neural oscillatory amplitude spectra from selected resting state networks of interest: (*A*) the default mode network, (*B*) the motor network, (*C*) visual areas, (*D*) the left frontoparietal network, (*E*) the right frontoparietal network, (*F*) medial frontal cortex, and (*G*) cerebellum.

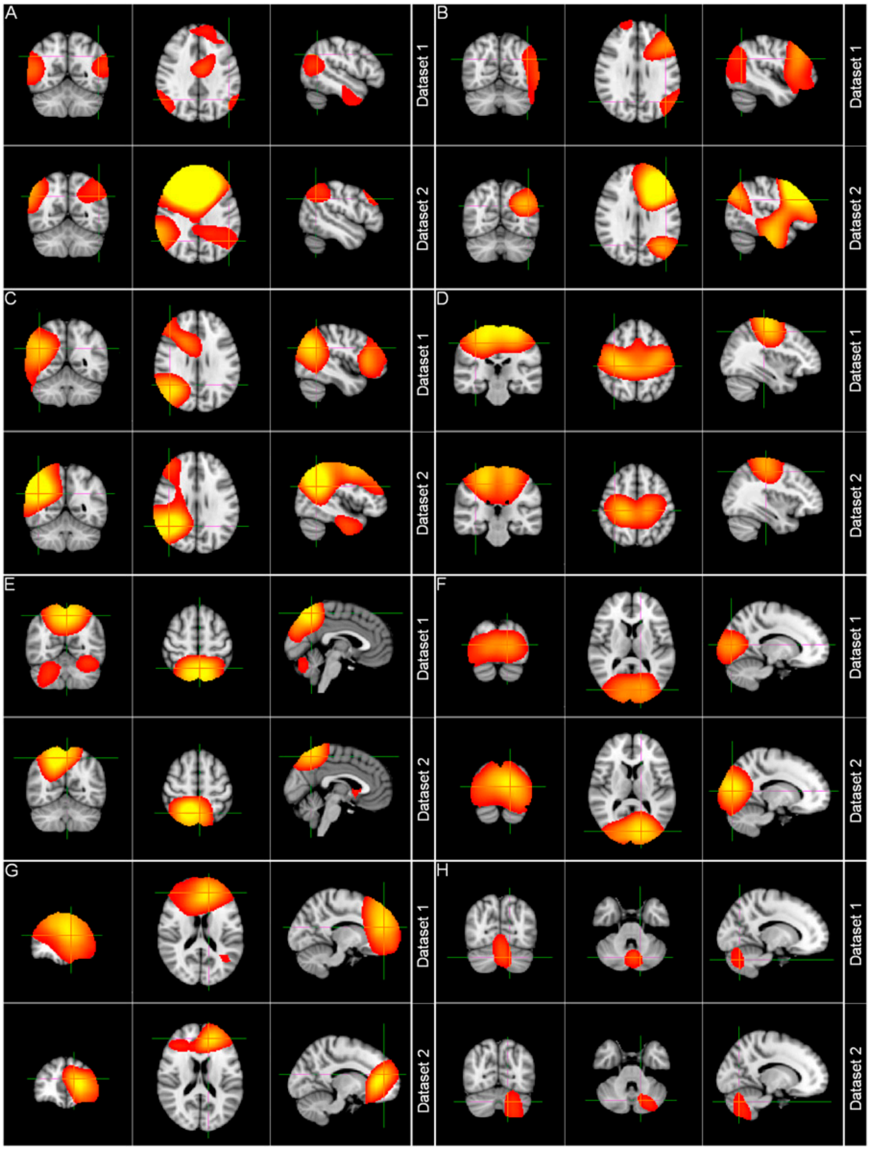

Fig. S7. Consistency of resting state networks in two multisubject MEG resting state datasets. *A–H* show spatial maps representing each of the networks depicted in Fig. 1 of the main text. *A–H*, *Upper* show the spatial structure of the RSN identified in the original 10-subject dataset (dataset 1, equivalent to those shown in Fig. 1). In *A–H*, *Lower* the results are derived from a separate dataset comprising 5-min resting state recordings in 14 subjects (dataset 2). (*A*) Default mode network (α); (*B*) left lateral frontoparietal network (β); (*C*) right lateral frontoparietal network (β); (*D*) motor network (β); (*E*) medial parietal regions (β); (*F*) visual network (β); (*G*) frontal lobes including anterior cingulate cortex (β); (*H*) cerebellum (β).

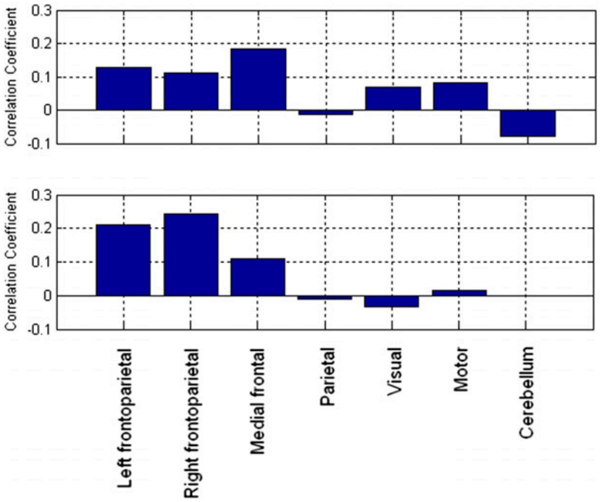

Fig. S8. Correlation measurements made between the time course of the DMN (α-band) and all of the other networks (identified in the β-band). *Upper*, the result for the original data (equivalent to Fig. 3*C* in the main text); *Lower*, the result for the comparison dataset.